

See discussions, stats, and author profiles for this publication at: <https://www.researchgate.net/publication/265094102>

# Electrical Detection of Spin-Polarized Surface States Conduction in $(\text{Bi}_{0.5}\text{Sb}_{0.47})_2\text{Te}_3$ Topological Insulator

ARTICLE in NANO LETTERS · AUGUST 2014

Impact Factor: 13.59 · DOI: 10.1021/nl5026198 · Source: PubMed

CITATIONS

18

READS

130

13 AUTHORS, INCLUDING:



Jianshi Tang

IBM

50 PUBLICATIONS 856 CITATIONS

SEE PROFILE



Li-Te Chang

University of California, Los Angeles

18 PUBLICATIONS 423 CITATIONS

SEE PROFILE



Mohammad Montazeri

University of California, Los Angeles

27 PUBLICATIONS 329 CITATIONS

SEE PROFILE



Yong Wang

University of Illinois at Chicago

249 PUBLICATIONS 2,456 CITATIONS

SEE PROFILE

# Electrical Detection of Spin-Polarized Surface States Conduction in $(\text{Bi}_{0.53}\text{Sb}_{0.47})_2\text{Te}_3$ Topological Insulator

Jianshi Tang,<sup>\*,†</sup> Li-Te Chang,<sup>†</sup> Xufeng Kou,<sup>†</sup> Koichi Murata,<sup>†</sup> Eun Sang Choi,<sup>‡</sup> Murong Lang,<sup>†</sup> Yabin Fan,<sup>†</sup> Ying Jiang,<sup>§</sup> Mohammad Montazeri,<sup>†</sup> Wanjun Jiang,<sup>†</sup> Yong Wang,<sup>§</sup> Liang He,<sup>\*,†</sup> and Kang L. Wang<sup>\*,†</sup>

<sup>†</sup>Device Research Laboratory, Department of Electrical Engineering, University of California, Los Angeles, California 90095, United States

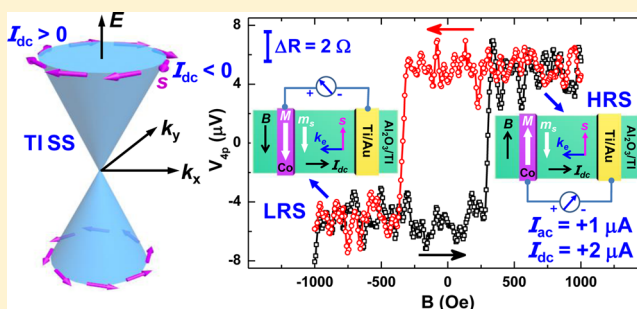
<sup>‡</sup>National High Magnetic Field Laboratory, Tallahassee, Florida 32310, United States

<sup>§</sup>Center for Electron Microscopy and State Key Laboratory of Silicon Materials, Department of Materials Science and Engineering, Zhejiang University, Hangzhou, 310027, China

## S Supporting Information

**ABSTRACT:** Strong spin–orbit interaction and time-reversal symmetry in topological insulators enable the spin-momentum locking for the helical surface states. To date, however, there has been little report of direct electrical spin injection/detection in topological insulator. In this Letter, we report the electrical detection of spin-polarized surface states conduction using a Co/ $\text{Al}_2\text{O}_3$  ferromagnetic tunneling contact in which the compound topological insulator  $(\text{Bi}_{0.53}\text{Sb}_{0.47})_2\text{Te}_3$  was used to achieve low bulk carrier density. Resistance (voltage) hysteresis with the amplitude up to about 10  $\Omega$  was observed when sweeping the magnetic field to change the relative orientation between the Co electrode magnetization and the spin polarization of surface states. The two resistance states were reversible by changing the electric current direction, affirming the spin-momentum locking in the topological surface states. Angle-dependent measurement was also performed to further confirm that the abrupt change in the voltage (resistance) was associated with the magnetization switching of the Co electrode. The spin voltage amplitude was quantitatively analyzed to yield an effective spin polarization of 1.02% for the surface states conduction in  $(\text{Bi}_{0.53}\text{Sb}_{0.47})_2\text{Te}_3$ . Our results show a direct evidence of spin polarization in the topological surface states conduction. It might open up great opportunities to explore energy-efficient spintronic devices based on topological insulators.

**KEYWORDS:** Topological insulator, spin polarization, surface states, spin-momentum locking, spin detection



Since the discovery of two-dimensional (2D) and three-dimensional (3D) topological insulators (TIs),<sup>1–5</sup> they have attracted extensive research interest for their exotic physical properties that could lead to dissipationless transport in the quantum spin Hall state.<sup>6–9</sup> Recent studies have shown a giant spin–orbit torque in TI originating from the strong spin–orbit interaction,<sup>10,11</sup> which enabled the current-induced magnetization switching through spin-transfer torque with a low current density. The unique feature of 3D TI, for instance, is that it has both insulating bulk and gapless Dirac surface states.<sup>8,9</sup> Ternary TI compounds, such as  $(\text{Bi}_x\text{Sb}_{1-x})_2\text{Te}_3$ , have been widely investigated for their tunability to achieve low bulk carrier density and manifest topological surface states conduction.<sup>12,13</sup> The presence of surface states is supported by extensive angle-resolved photoemission spectroscopy (ARPES) measurements and transport studies,<sup>14–20</sup> such as Shubnikov-de Haas (SdH) and Aharonov Bohm (AB) quantum oscillations. Because of the strong spin–orbital interaction in TI, direct back scatterings from nonmagnetic impurities are

prohibited by the time-reversal symmetry.<sup>8,9</sup> More importantly, the spin-momentum locking naturally leads to a current-induced spin polarization in surface states;<sup>21</sup> the surface states conduction is spin-polarized once an electric current is passed through a TI film, and this spin polarization can be accordingly reversed by simply flipping the electric current direction.<sup>22,23</sup> As a result, it has been proposed to use TI as a promising spin injection source to inject spin-polarized carriers into non-magnetic materials, such as metal and graphene.<sup>24–26</sup>

The presence of spin-polarized surface states has been mainly examined using optical methods. For example, spin-resolved ARPES has been widely used to resolve the helical spin texture at different energy levels,<sup>14–16</sup> and the spin texture is found to be opposite for above and below the Dirac point.<sup>15</sup> Another approach is to use circularly polarized light to excite spin-

Received: July 10, 2014

Revised: August 24, 2014

Published: August 26, 2014

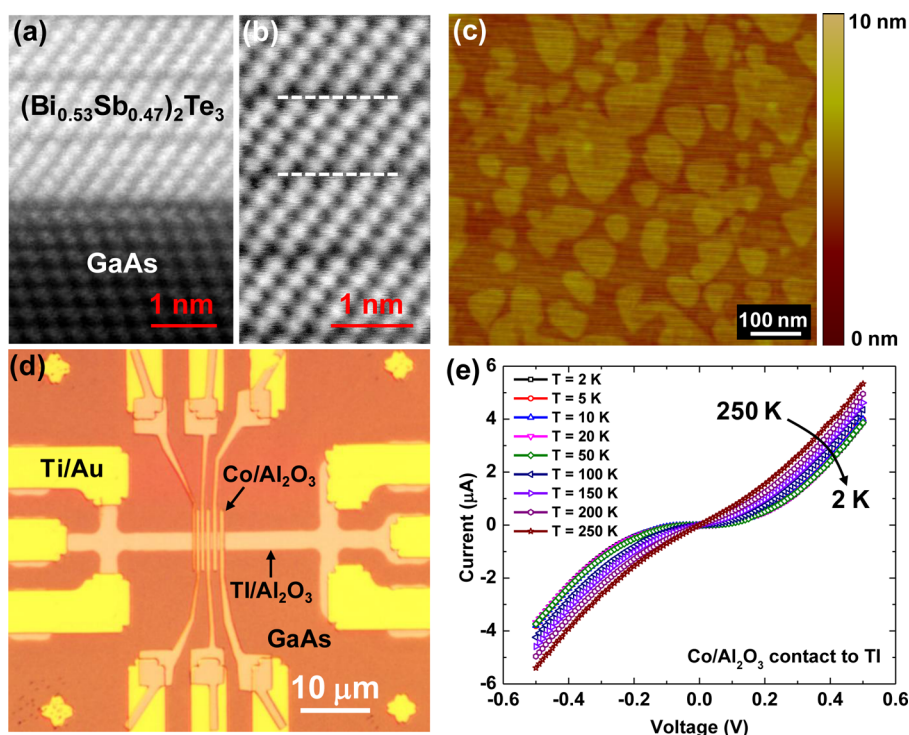


**Figure 1.** Film property and device structure for spin detection in TI. (a) High-resolution cross-sectional TEM image of  $(\text{Bi}_{0.53}\text{Sb}_{0.47})_2\text{Te}_3$  thin film grown on a GaAs substrate with an atomically clean interface. (b) Magnified picture showing the details of the van der Waals gaps. Each quintuple layer with the van der Waals gap is well resolved, as labeled by the white dash lines. (c) AFM image of the  $\text{Al}_2\text{O}_3$ -capped  $(\text{Bi}_{0.53}\text{Sb}_{0.47})_2\text{Te}_3$  film, showing a relatively smooth surface morphology. (d) Microscope image of the as-fabricated TI Hall-bar device with  $\text{Co}/\text{Al}_2\text{O}_3$  ferromagnetic tunneling contacts on the channel. (e) Temperature-dependent  $I$ - $V$  curves measured from the  $\text{Co}/\text{Al}_2\text{O}_3$  contact on the TI channel. The nonlinear  $I$ - $V$  characteristics with weak temperature dependence suggest tunneling transport through the 1.2 nm  $\text{Al}_2\text{O}_3$ .

polarized photocurrent in TI surface states.<sup>27–29</sup> Left- and right-circularly polarized light selectively interacts with opposite spin polarizations with components that are either parallel or antiparallel to the wave vector of the incident light.<sup>27</sup> However, there has been little report of direct electrical injection or detection in TI. Very recently, the electrical detection of charge-current-induced spin polarization was reported in  $\text{Bi}_2\text{Se}_3$ , and the spin polarization was estimated to be 0.2 per unit current based on a quantum transport model.<sup>30,31</sup> Although  $\text{Bi}_2\text{Se}_3$  has a large bulk band gap of about 0.3 eV, it is known that there are excessive Se vacancies in  $\text{Bi}_2\text{Se}_3$  that can result in a degenerately high  $n$ -type doping density ( $n_{2\text{D}} = 10^{13} \sim 10^{14} \text{ cm}^{-2}$ ), which places the Fermi level within the bulk conduction band.<sup>32</sup> The coexistence of topological surface states and two-dimensional electron gas with a large tunable Rashba spin splitting on the surface of  $\text{Bi}_2\text{Se}_3$  would complicate the spin texture.<sup>33</sup> To circumvent this problem, we intentionally chose the compound TI  $(\text{Bi}_x\text{Sb}_{1-x})_2\text{Te}_3$  in this work and carefully tuned the composition ( $x = 0.53$ ) to achieve the lowest bulk carrier density ( $n_{2\text{D}} \sim 10^{12} \text{ cm}^{-2}$ ) with a clean spin texture.<sup>12</sup> The electrical detection of the spin-polarized topological surface states conduction was carried out using one ferromagnetic contact as the spin detector to probe the spin polarization. In addition, a tunneling barrier was used to enhance the spin detection efficiency.<sup>34</sup> It should be pointed out that standard spin injection/detection measurement setup may not be feasible to study the spin transport in TI (Supporting Information S1) because the spin diffusion length in TI is expected to be extremely small because of the strong spin–orbital interaction.<sup>22</sup> Also, the typical ferromagnetic spin injector is not needed here as the spin polarization in the

topological surface states conduction is inherently provided by the spin-momentum locking.<sup>8,9</sup>

**Device Structure and Characterizations.** To start, eight quintuple layers of  $(\text{Bi}_{0.53}\text{Sb}_{0.47})_2\text{Te}_3$  TI thin film were grown on a high-resistivity GaAs (111)B substrate using molecular beam epitaxy (MBE).<sup>12,35</sup> The layer-by-layer growth was in situ monitored by the reflection high-energy electron diffraction (RHEED) pattern (see Supporting Information S2). Although reducing the film thickness could diminish the bulk conduction and hence enhance the surface states signal,<sup>30</sup> the hybridization between the top and bottom surface states would open a gap at the Dirac point, which transforms massless Dirac Fermions to massive Fermions and might also change the spin texture in TI.<sup>36</sup> Therefore, the thickness of eight quintuple layers in our sample was intentionally chosen to minimize the bulk conductance while avoiding the interaction between the two topological surfaces. The Bi and Sb atomic ratio was fine-tuned to reach the lowest bulk carrier density, where the Fermi level lied within the bulk band gap.<sup>13</sup> A 0.8 nm thick Al layer was in situ deposited on top after the growth to cap the  $(\text{Bi}_{0.53}\text{Sb}_{0.47})_2\text{Te}_3$  surface and to prevent any environment doping and surface oxidation.<sup>37,38</sup> After being taken out from the chamber and exposed to air, the Al capping layer was naturally oxidized into  $\text{Al}_2\text{O}_3$  with a thickness of about 1.2 nm, which served as the tunneling barrier for the ferromagnetic contact. This method has been widely used to produce the tunneling barrier for electrical spin injection and detection studies in various materials.<sup>30,39,40</sup> A high-resolution transmission electron microscope (HRTEM) was used to investigate the TI film quality. As shown in Figure 1a,b, the HRTEM cross-sectional image demonstrated an abrupt and clean epitaxial

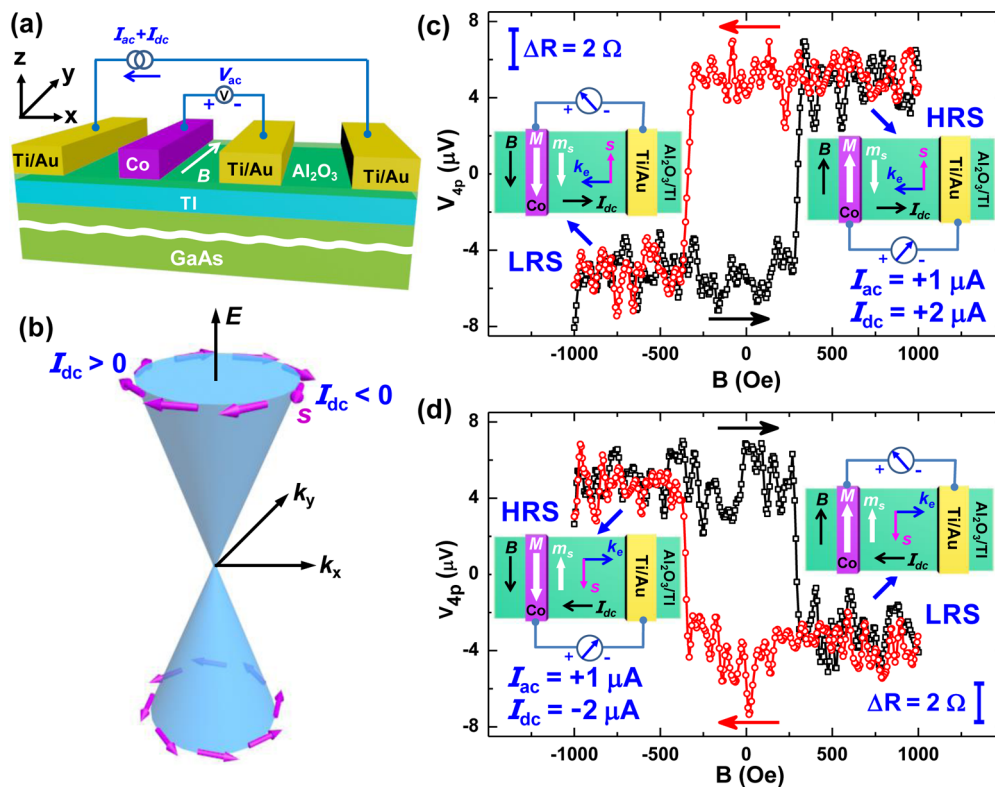


**Figure 2.** Electrical detection of the spin-polarized surface states conduction in  $(\text{Bi}_{0.53}\text{Sb}_{0.47})_2\text{Te}_3$ . (a) Schematic illustration of the device structure with one ferromagnetic tunneling  $\text{Co}/\text{Al}_2\text{O}_3$  contact for spin detection. The measurement setup with a 4-probe configuration and a lock-in technique is also illustrated. (b) Schematic illustration of the helical spin texture of the surface states in TI: clockwise spin texture (left-handed chirality) above the Dirac point while counterclockwise spin texture (right-handed chirality) below the Dirac point. (c,d) The measured voltage (resistance) at  $T = 1.9$  K as the in-plane magnetic field is swept back and forth under dc bias of  $I_{dc} = +2 \mu\text{A}$  and  $I_{dc} = -2 \mu\text{A}$ , respectively. The parabolic background MR was subtracted. The scale bar represents a corresponding resistance change of  $2 \Omega$ . The red and black arrows indicate the magnetic field sweeping direction. The insets show the HRS and LRS, determined by the relative orientation between the Co electrode magnetization  $M$  and the spin polarization  $s$  of surface states. The electron spin  $s$  is antiparallel to its magnetic moment  $m_s$  because of the negative charge of electron.

interface of  $(\text{Bi}_{0.53}\text{Sb}_{0.47})_2\text{Te}_3$  on the GaAs substrate and each quintuple layer with the van der Waals gap was well resolved. The chemical composition was confirmed by the Bi, Sb, and Te peaks in the energy-dispersive spectrum (EDS) collected from the  $(\text{Bi}_{0.53}\text{Sb}_{0.47})_2\text{Te}_3$  film (see Supporting Information S3). The atomic force microscope (AFM) image was also taken on the  $(\text{Bi}_{0.53}\text{Sb}_{0.47})_2\text{Te}_3$  film and showed a relatively smooth surface morphology in Figure 1c. The estimated root-mean-square (RMS) surface roughness was about 0.57 nm.

After the growth, the  $(\text{Bi}_{0.53}\text{Sb}_{0.47})_2\text{Te}_3$  film was patterned into standard Hall bar structures with 10 nm/100 nm thick Ti/Au nonmagnetic contacts and  $\text{Co}/\text{Al}_2\text{O}_3$  ferromagnetic contacts. The 40 nm thick Co contacts were defined by electron beam lithography and electron beam evaporation and another layer of 5 nm  $\text{Al}_2\text{O}_3$  was also evaporated in situ to prevent subsequent oxidation of the Co electrodes. The microscope image of the final device for spin detection is shown in Figure 1d. To verify the tunneling nature of the  $\text{Co}/\text{Al}_2\text{O}_3$  contact to the  $(\text{Bi}_{0.53}\text{Sb}_{0.47})_2\text{Te}_3$  channel, temperature-dependent  $I$ – $V$  measurements were performed from 2 to 250 K, as shown in Figure 1e. The nonlinear  $I$ – $V$  characteristics and relatively weak temperature dependence clearly indicate tunneling dominant transport through the 1.2 nm  $\text{Al}_2\text{O}_3$  barrier,<sup>41</sup> which is essential to enhance the spin detection efficiency (see Supporting Information S5 for further discussion on the temperature dependence).<sup>34,42</sup> The ferromagnetism of the Co electrode was also verified by the magneto-optic Kerr

effect (MOKE) measurement on a Co film, which was deposited at the same time with the Co electrode (see Supporting Information S6).

**Detection of Spin-Polarized Surface States Conduction.** Figure 2a shows the schematic device structure and measurement setup for the electrical detection of spin-polarized surface states conduction in  $(\text{Bi}_{0.53}\text{Sb}_{0.47})_2\text{Te}_3$ . Here two outer nonmagnetic contacts (Ti/Au) were used to pass electric current (along the  $x$ -axis) through the TI channel, while one ferromagnetic tunneling contact ( $\text{Co}/\text{Al}_2\text{O}_3$ ) was used to detect the spin polarization of the surface states conduction. A lock-in technique was employed to increase the signal-to-noise ratio, and a 4-probe configuration was also adopted to exclude the contact resistance and any spurious signals from the contact. The low-temperature transport measurements were performed using a Quantum Design Physical Property Measurement System (PPMS) connected with Keithley 6221 AC/DC current source and lock-in amplifier SR830. An in-plane magnetic field was applied along the easy axis ( $y$ -axis) of the Co electrode to control its magnetization direction. Meanwhile, the spin polarization direction of the surface states conduction was determined by the electric current direction and the spin-momentum locking. It should be pointed out that the electron spin  $s$  is antiparallel to its magnetic moment  $m_s$  because of the negative charge of electron.<sup>43</sup> In our  $(\text{Bi}_{0.53}\text{Sb}_{0.47})_2\text{Te}_3$  film, the Fermi level is above the Dirac point,<sup>13</sup> so the spin texture of surface states is expected to be clockwise (left-handed chirality)



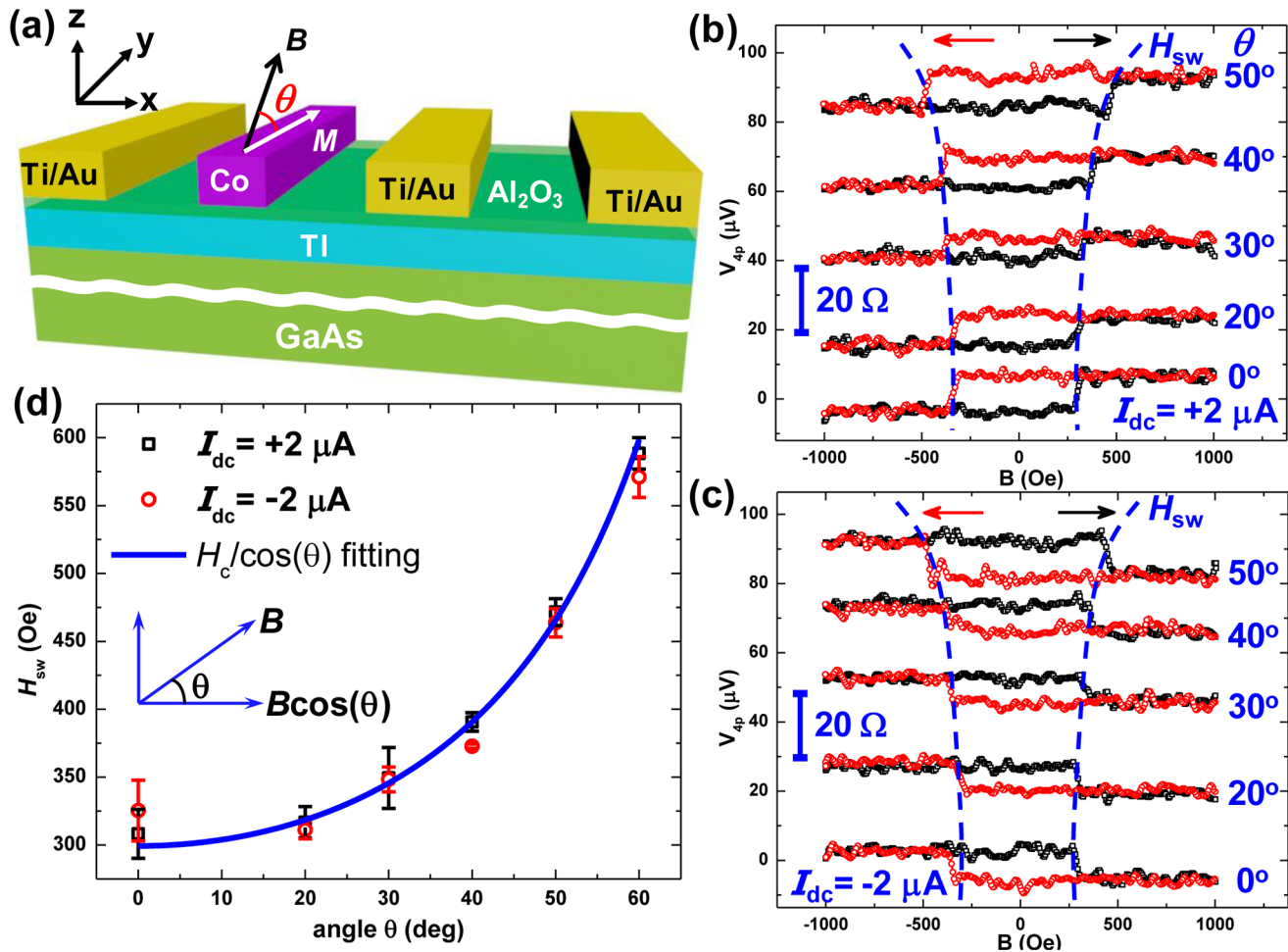


**Figure 3.** Angle-dependent measurements. (a) Schematic illustration of the magnetic field (black arrow) rotation in the  $y$ - $z$  plane. (b,c) Voltage hysteresis curves at different rotation angles under dc bias of  $I_{dc} = +2 \mu A$  and  $I_{dc} = -2 \mu A$ , respectively. The red and black arrows indicate the magnetic field sweeping direction. The parabolic MR background was subtracted in all the curves. The curves are intentionally offset for clarity, and the scale bar represents a corresponding resistance change of  $20 \Omega$ . The blue dash lines mark the switching fields increasing with rotation angle. (d) The extracted switching fields (data points) at different rotation angles is well fitted by the  $H_c/\cos(\theta)$  relation (blue line), indicating only the magnetic field component along the  $y$ -axis determines the magnetization switching of the Co electrode. The error bars are calculated from positive and negative switching fields in multiple measurements.

from the previous spin-resolved ARPES measurements as illustrated in Figure 2b,<sup>14–16</sup> that is, the spin polarization  $s$  is pointing along  $-y$  direction for momentum ( $k_x > 0, k_y = 0$ ), while along  $+y$  direction for momentum ( $k_x < 0, k_y = 0$ ). Figure 2c shows the measured hysteresis of the measured voltage at  $T = 1.9$  K as the in-plane magnetic field was swept back and forth under a constant ac current of  $I_{ac} = 1 \mu A$  plus a dc bias of  $I_{dc} = +2 \mu A$ . For clarity, the trivial parabolic magnetoresistance (MR) background, originating from the  $(Bi_{0.53}Sb_{0.47})_2Te_3$  channel between the two voltage probes, was subtracted (see Supporting Information S7 for the raw data). The measured voltage (resistance) depends on the relative orientation between the surface states spin polarization and the Co electrode magnetization: a low resistance state (LRS) when the electron magnetic moment  $m_s$  was parallel to the Co magnetization  $M$  (hence  $s$  was antiparallel to  $M$ ), and a high resistance state (HRS) when  $m_s$  was antiparallel to  $M$  (hence  $s$  was parallel to  $M$ ). Such configuration is analogous to that in a typical magnetic tunnel junction (MTJ), in which the junction resistance is determined by the relative magnetization orientation between the two ferromagnetic layers. The abrupt change in the voltage (resistance) corresponded to the

magnetization switching of the Co electrode (with a width of about 400 nm) at the coercive field of about  $H_c \sim 300$  Oe, which was estimated from the anisotropic magnetoresistance (AMR) measurement (see Supporting Information S8). The inset shows the schematic illustration of the relative orientation between the surface states spin polarization and the Co electrode magnetization (for  $I_{dc} = +2 \mu A$ ): HRS for positive magnetic field ( $M // -m_s // s$ ) while LRS for negative magnetic field ( $M // m_s // -s$ ). It is noted that the HRS and LRS in our voltage hysteresis is shown opposite from that observed in  $Bi_2Se_3$ ,<sup>30</sup> however, the interpreted spin texture in this way is consistent with the reported spin-resolved APRES data as illustrated in Figure 2b.<sup>14–16</sup> Furthermore, if the electric current direction was flipped to  $I_{dc} = -2 \mu A$ , then the LRS and HRS were also reversed,<sup>30</sup> as shown in Figure 2d: LRS for positive magnetic field ( $M // m_s // -s$ ) while HRS for negative magnetic field ( $M // -m_s // s$ ). More than 10  $(Bi_{0.53}Sb_{0.47})_2Te_3$  devices have been measured, and the current-reversible voltage hysteresis was observed in multiple samples. This result directly demonstrates the spin-momentum locking feature for the surface states conduction in TI. It should be pointed out that this current-reversible hysteresis cannot originate from the Co

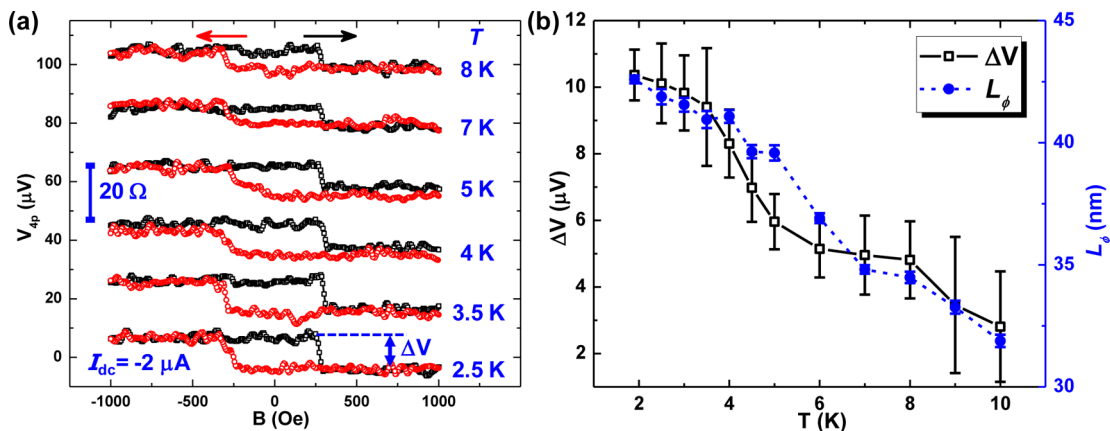


**Figure 4.** Temperature dependence of the spin signal. (a) Temperature-dependent voltage hysteresis curves under dc bias of  $I_{dc} = -2 \mu\text{A}$ . The red and black arrows indicate the magnetic field sweeping direction. The parabolic MR background was subtracted in all the curves. The curves are intentionally offset for clarity, and the scale bar represents a corresponding resistance change of  $20 \Omega$ . (b) Extracted spin voltage signal amplitude at different temperatures up to 10 K. In general, the signal amplitude decreases as the temperature increases, indicating the reduction of effective spin polarization of the total current. The error bars are calculated from forward and backward sweeps of the magnetic field in multiple measurements. The temperature-dependent phase coherence length from the HLN fitting of the low-field magneto-conductivity is also plotted, showing similar temperature dependence.

contact itself due to effects including AMR, tunneling anisotropic magnetoresistance (TAMR) and anomalous Hall effect (AHE).<sup>30,44–46</sup> To further rule out those effects, control experiments have been carried out on another sample without the  $\text{Al}_2\text{O}_3$  layer, in which no hysteresis was observed (see Supporting Information S8 and S9).

**Angle-Dependent Measurements.** To further verify that the hysteresis is closely correlated with the magnetization switching of the Co electrode, the magnetic field was rotated in the  $y$ - $z$  plane toward the out-of-plane direction. As illustrated in Figure 3a, there is an angle  $\theta$  between the applied magnetic field (in the  $y$ - $z$  plane) and the easy  $y$ -axis of the Co electrode. Figure 3b,c shows the voltage hysteresis curves at different rotation angles  $\theta$  under dc bias of  $I_{dc} = +2 \mu\text{A}$  and  $I_{dc} = -2 \mu\text{A}$ , respectively. Again the trivial parabolic MR background was subtracted in all the curves for clarity. The switching field  $H_{sw}$  was found to increase with the rotation angle for both bias conditions, and the hysteresis completely vanished as the rotation angle approached  $\theta = 90^\circ$ . Figure 3d further plots the switching field  $H_{sw}$  as a function of the rotation angle  $\theta$ , which can be well fitted with the  $H_c/\cos(\theta)$  relation. This result suggests that the abrupt change in the voltage (resistance) occurred when the in-plane component (along the easy  $y$ -axis) of the applied magnetic field reached the coercive field of the Co electrode, that is, the magnetization switching of the Co electrode. Therefore, the abrupt switching between the LRS and the HRS in the voltage (resistance) hysteresis was indeed correlated with the change in the relative orientation between the surface states spin polarization and the Co electrode magnetization. It should be pointed out that the out-of-plane component of the applied magnetic field (less than 1 kOe) was much smaller than the Co saturation field along the hard  $z$ -axis (typically tens of kOe), hence it did not change the Co magnetization orientation but only contributed to the parabolic MR background. In addition, the small out-of-plane magnetic field did not affect the surface states because that the induced gap opening in the surface states was negligible.<sup>47</sup>

**Analysis of the Spin Polarization.** Furthermore, temperature-dependent voltage hysteretic data were measured from 1.9 to 10 K, and the results are shown in Figure 4a for the bias

of  $I_{dc} = -2 \mu\text{A}$ . We can further define the spin voltage amplitude as  $\Delta V = V_{AP} - V_P = I_{ac}(R_{AP} - R_P)$ , in which  $V_{AP}$  ( $R_{AP}$ ) and  $V_P$  ( $R_P$ ) represent the measured voltage (resistance) in the HRS and LRS, respectively. The temperature-dependent spin voltage amplitude is plotted in Figure 4b. Overall, the spin signal amplitude decreases as the temperature increases,<sup>30</sup> suggesting that the effective spin polarization of the total current decreases. This could be attributed to the fact that with the temperature increasing: (1) the bulk conduction increases due to thermally activated bulk dopants, so that the relative contribution from the spin-polarized surface states conduction decreases;<sup>48</sup> (2) inelastic scatterings such as phonon scatterings increase so that the spin polarization of surface states conduction also decreases. To explain the temperature dependence of the surface states conduction more clearly, standard magneto-transport measurements were performed on the Hall bar structure patterned on the same  $(\text{Bi}_{0.53}\text{Sb}_{0.47})_2\text{Te}_3$  film (see Figure 1d for the device structure and dimension). In the Hall measurements, the longitudinal resistance ( $R_{xx}$ ) and transverse resistance ( $R_{xy}$ ) were measured when sweeping the out-of-plane magnetic field. The low-field magneto-conductivity was fitted by the standard Hikami–Larkin–Nagaoka (HLN) theory in the temperature range between 1.9 and 10 K (see Supporting Information S10).<sup>37,49,50</sup> The extracted phase coherence length is then plotted in Figure 4b, which shows a similar temperature dependence as the measured spin voltage amplitude. The phase coherence length decreased with increasing temperature, indicating that the surface states conduction diminished.

To quantitatively estimate the spin polarization of the surface state conduction in the  $(\text{Bi}_{0.53}\text{Sb}_{0.47})_2\text{Te}_3$ , we established a model similar to that in standard spin injection and detection in semiconductors (see Supporting Information S1 and S11). The measured voltage difference  $\Delta V = V_{AP} - V_P$  can be interpreted to probe the electrochemical potential (quasi Fermi level) difference between the majority and minority spin directions<sup>51</sup>

$$\Delta V = \alpha \frac{\gamma_{P_{Co}}}{e} \Delta\mu \quad (1)$$

where  $\alpha = \sigma_{\text{SS}}/\sigma_{\text{total}}$  is the surface conductance ratio,  $\gamma$  is the spin detection efficiency through the  $\text{Co}/\text{Al}_2\text{O}_3$  tunneling contact,  $P_{\text{Co}} = (n_{\text{Co}\uparrow} - n_{\text{Co}\downarrow})/(n_{\text{Co}\uparrow} + n_{\text{Co}\downarrow})$  is the spin polarization of the Co electrode with  $n_{\text{Co}\uparrow}(n_{\text{Co}\downarrow})$  being the electron density with the majority (minority) spin direction,  $\Delta\mu = \mu_{\uparrow} - \mu_{\downarrow}$  is the splitting in the spin-dependent electrochemical potential between the majority and minority spin directions, which can be further derived as

$$\begin{aligned}\Delta\mu &= \frac{n_{\text{SS}\uparrow} - n_{\text{SS}\downarrow}}{N(E_{\text{F}})} \\ &= \left( \frac{n_{\text{SS}\uparrow} - n_{\text{SS}\downarrow}}{n_{\text{SS}\uparrow} + n_{\text{SS}\downarrow}} \right) \left( \frac{n_{\text{SS}\uparrow} + n_{\text{SS}\downarrow}}{N(E_{\text{F}})} \right) \\ &= P_{\text{SS}} \left( \frac{n_{\text{total}}}{N(E_{\text{F}})} \right)\end{aligned}\quad (2)$$

where  $P_{\text{SS}} = (n_{\text{SS}\uparrow} - n_{\text{SS}\downarrow})/(n_{\text{SS}\uparrow} + n_{\text{SS}\downarrow})$  is the effective spin polarization of the surface states conduction,  $N(E_{\text{F}})$  is the density of states at the Fermi level. For the 2D Dirac surface states with a linear  $E-k$  relation, the density of states is proportional to the energy as  $N(E) = |E|/[\pi(\hbar v_{\text{F}})^2]$  in which  $\hbar$  is the reduced Planck's constant and  $v_{\text{F}}$  is the Fermi velocity.<sup>52</sup> Then by integration in the energy space

$$n_{\text{total}} = \int_0^{E_{\text{F}}} N(E) dE = \frac{1}{2} E_{\text{F}} N(E_{\text{F}}) \quad (3)$$

we can rewrite the spin voltage amplitude as

$$\Delta V = \alpha \frac{\gamma P_{\text{Co}} E_{\text{F}}}{2e} P_{\text{SS}} \quad (4)$$

From our measurement results shown in Figure 4b,  $\Delta V = (10.4 \pm 0.8) \mu\text{V}$  at  $T = 1.9$  K. Using the values of  $\alpha = \sigma_{\text{SS}}/\sigma_{\text{total}} = 53\%$ ,  $E_{\text{F}} = 83$  meV estimated from the SdH oscillations in the longitudinal resistance  $R_{\text{xx}}$  (see Supporting Information S4), and  $P_{\text{Co}} = 42\%$ ,<sup>53</sup>  $\gamma = 11\%$  for the  $\text{Co}/\text{Al}_2\text{O}_3$  tunnel junction from literature,<sup>42</sup> we can then calculate the effective spin polarization of the surface states conduction in  $(\text{Bi}_{0.53}\text{Sb}_{0.47})_2\text{Te}_3$  to be  $P_{\text{SS}} = (1.02 \pm 0.08)\%$ . This is smaller than the theoretical predication of about 50% spin polarization for the 3D TI surface states from first-principle calculations.<sup>21</sup> Such deviation can be probably attributed to that the dimension of the top surface in our device (in micron scale) is much larger than the typical mean-free path and phase coherence length (tens to hundreds nanometers, see Supporting Information S10),<sup>17,18,37</sup> hence the carrier transport through the surface states suffers from considerable scatterings. Another possible reason could be the overestimation of the spin detection efficiency in the nonideal  $\text{Co}/\text{Al}_2\text{O}_3$  tunneling contact, considering that the  $(\text{Bi}_{0.53}\text{Sb}_{0.47})_2\text{Te}_3$  surface has a terrace-like morphology. The spin injection/detection process is known to be very sensitive to the surface roughness, which would induce interface traps or local magnetostatic fields that could dramatically affect the spin detection process.<sup>54</sup> In addition, the potential contribution from the bulk states (especially the Rashba spin-splitting states with an opposite spin texture to the topological surface states) could also lower the observed spin polarization. To further enhance the spin signal and spin polarization in the future, one effective approach according to eq 4 is to tune the Fermi energy and to enhance the surface conductance ratio, which can be achieved through doping and gate control.<sup>12,35</sup> Besides, improving the TI film

quality (e.g., surface morphology) could also help enhance the observed spin signal.

To sum up, we have successfully demonstrated the electrical detection of spin-polarized surface states conduction in the  $(\text{Bi}_{0.53}\text{Sb}_{0.47})_2\text{Te}_3$  TI film using a  $\text{Co}/\text{Al}_2\text{O}_3$  ferromagnetic tunneling contact. By changing the directions of both the magnetic field and the electric current, reversible voltage (resistance) hysteresis was observed up to 10 K, in which the HRS and LRS were obtained from the relative orientation between the Co magnetization and the spin polarization of topological surface states. It was further verified by angle-dependent measurements that the abrupt change in the voltage (resistance) indeed corresponded to the magnetization switching of the Co electrode. These transport results affirmed the spin-momentum locking feature of the topological surface states enabled by the strong spin-orbit interaction and the time-reversal symmetry in TI. The spin voltage amplitude was quantitatively analyzed to yield an effective spin polarization of about 1.02% for the surface states conduction in  $(\text{Bi}_{0.53}\text{Sb}_{0.47})_2\text{Te}_3$ . The measured low spin polarization could be attributed to the short mean-free path and phase coherence length in TI and the terrace-like TI surface morphology that limits the spin detection efficiency. From our analysis, it is suggested that this value can be further enhanced by tuning the Fermi level and increasing the surface states conduction ratio. Our findings demonstrated an exotic feature of spin-polarized surface states in TI from electrical transport measurements. The present results may pave the road to explore innovative energy-efficient spintronic devices based on TIs.

## ■ ASSOCIATED CONTENT

### Supporting Information

Spin detection in conventional semiconductors and topological insulator, RHEED pattern and oscillation, EDS spectrum of the  $(\text{Bi}_{0.53}\text{Sb}_{0.47})_2\text{Te}_3$  film, low-temperature transport measurements, temperature-dependent resistance of the  $\text{Co}/\text{Al}_2\text{O}_3$  contact, MOKE signal of Co film, raw data of the measured 4-probe resistance, AMR measurement on the Co contact, control experiment without the  $\text{Al}_2\text{O}_3$  layer, HLN fitting of the phase coherence length in  $(\text{Bi}_{0.53}\text{Sb}_{0.47})_2\text{Te}_3$ , discussion on the quantum transport model, and Hall data of the  $(\text{Bi}_{0.53}\text{Sb}_{0.47})_2\text{Te}_3$  film. This material is available free of charge via the Internet at <http://pubs.acs.org>.

## ■ AUTHOR INFORMATION

### Corresponding Authors

\*E-mail: (J.T.) [tjianshi@ucla.edu](mailto:tjianshi@ucla.edu).

\*E-mail: (L.H.) [liang.heliang@gmail.com](mailto:liang.heliang@gmail.com).

\*E-mail: (K.L.W.) [wang@seas.ucla.edu](mailto:wang@seas.ucla.edu).

### Notes

The authors declare no competing financial interest.

## ■ ACKNOWLEDGMENTS

The authors acknowledge insightful discussions from the Device Research Laboratory at UCLA. The authors also acknowledge the support from Defense Advanced Research Projects Agency (DARPA) with Grants N66001-12-1-4034 and N66001-11-1-4105, and the Function Accelerated nanoMaterial Engineering (FAME) center. A portion of this work was performed at the National High Magnetic Field Laboratory, which is supported by NSF Cooperative Agreement No. DMR-1157490, by the State of Florida, and by the Department of



Energy (DOE). K.W. acknowledges the support of the Raytheon endowed chair professorship. Y.W. acknowledges the support from Natural Science Foundation of China (11174244) and Zhejiang Provincial Natural Science Foundation of China (LR12A04002) and National Young 1000 Talents Plan.

## REFERENCES

- (1) Fu, L.; Kane, C. L.; Mele, E. J. *Phys. Rev. Lett.* **2007**, *98*, 106803.
- (2) Fu, L.; Kane, C. L. *Phys. Rev. B* **2007**, *76*, 045302.
- (3) Bernevig, B. A.; Hughes, T. L.; Zhang, S.-C. *Science* **2006**, *314*, 1757–1761.
- (4) Zhang, H.; Liu, C.-X.; Qi, X.-L.; Dai, X.; Fang, Z.; Zhang, S.-C. *Nat. Phys.* **2009**, *5*, 438–442.
- (5) Chen, Y. L.; Analytis, J. G.; Chu, J.-H.; Liu, Z. K.; Mo, S.-K.; Qi, X. L.; Zhang, H. J.; Lu, D. H.; Dai, X.; Fang, Z.; Zhang, S. C.; Fisher, I. R.; Hussain, Z.; Shen, Z.-X. *Science* **2009**, *325*, 178–181.
- (6) König, M.; Wiedmann, S.; Brune, C.; Roth, A.; Buhmann, H.; Molenkamp, L. W.; Qi, X.-L.; Zhang, S.-C. *Science* **2007**, *318*, 766–770.
- (7) Chang, C.-Z.; Zhang, J.; Feng, X.; Shen, J.; Zhang, Z.; Guo, M.; Li, K.; Ou, Y.; Wei, P.; Wang, L.-L.; Ji, Z.-Q.; Feng, Y.; Ji, S.; Chen, X.; Jia, J.; Dai, X.; Fang, Z.; Zhang, S.-C.; He, K.; Wang, Y.; Lu, L.; Ma, X.-C.; Xue, Q.-K. *Science* **2013**, *340*, 167–170.
- (8) Hasan, M. Z.; Kane, C. L. *Rev. Mod. Phys.* **2010**, *82*, 3045–3067.
- (9) Hasan, M. Z.; Moore, J. E. *Annu. Rev. Condens. Matter Phys.* **2011**, *2*, 55–78.
- (10) Fan, Y.; Upadhyaya, P.; Kou, X.; Lang, M.; Takei, S.; Wang, Z.; Tang, J.; He, L.; Chang, L.-T.; Montazeri, M.; Yu, G.; Jiang, W.; Nie, T.; Schwartz, R. N.; Tserkovnyak, Y.; Wang, K. L. *Nat. Mater.* **2014**, *13*, 699–704.
- (11) Mellnik, A. R.; Lee, J. S.; Richardella, A.; Grab, J. L.; Mintun, P. J.; Fischer, M. H.; Vaezi, A.; Manchon, A.; Kim, E.-A.; Samarth, N.; Ralph, D. C. *Nature* **2014**, *511*, 449–451.
- (12) He, L.; Kou, X.; Lang, M.; Choi, E. S.; Jiang, Y.; Nie, T.; Jiang, W.; Fan, Y.; Wang, Y.; Xiu, F.; Wang, K. L. *Sci. Rep.* **2013**, *3*, 3406.
- (13) Kong, D.; Chen, Y.; Cha, J. J.; Zhang, Q.; Analytis, J. G.; Lai, K.; Liu, Z.; Hong, S. S.; Koski, K. J.; Mo, S.-K.; Hussain, Z.; Fisher, I. R.; Shen, Z.-X.; Cui, Y. *Nat. Nanotechnol.* **2011**, *6*, 705–709.
- (14) Hsieh, D.; Xia, Y.; Qian, D.; Wray, L.; Dil, J. H.; Meier, F.; Osterwalder, J.; Patthey, L.; Checkelsky, J. G.; Ong, N. P.; Fedorov, A. V.; Lin, H.; Bansil, A.; Grauer, D.; Hor, Y. S.; Cava, R. J.; Hasan, M. Z. *Nature* **2009**, *460*, 1101–1105.
- (15) Xu, S.-Y.; Xia, Y.; Wray, L. A.; Jia, S.; Meier, F.; Dil, J. H.; Osterwalder, J.; Slomski, B.; Bansil, A.; Lin, H.; Cava, R. J.; Hasan, M. Z. *Science* **2011**, *332*, 560–564.
- (16) Xia, Y.; Qian, D.; Hsieh, D.; Wray, L.; Pal, A.; Lin, H.; Bansil, A.; Grauer, D.; Hor, Y. S.; Cava, R. J.; Hasan, M. Z. *Nat. Phys.* **2009**, *5*, 398–402.
- (17) Qu, D.-X.; Hor, Y. S.; Xiong, J.; Cava, R. J.; Ong, N. P. *Science* **2010**, *329*, 821–824.
- (18) Xiu, F.; He, L.; Wang, Y.; Cheng, L.; Chang, L.-T.; Lang, M.; Huang, G.; Kou, X.; Zhou, Y.; Jiang, X.; Chen, Z.; Zou, J.; Shailos, A.; Wang, K. L. *Nat. Nanotechnol.* **2011**, *6*, 216–221.
- (19) Peng, H.; Lai, K.; Kong, D.; Meister, S.; Chen, Y.; Qi, X.-L.; Zhang, S.-C.; Shen, Z.-X.; Cui, Y. *Nat. Mater.* **2009**, *9*, 225–229.
- (20) Pan, Z. H.; Vescovo, E.; Fedorov, A. V.; Gardner, D.; Lee, Y. S.; Chu, S.; Gu, G. D.; Valla, T. *Phys. Rev. Lett.* **2011**, *106*, 257004.
- (21) Yazyev, O. V.; Moore, J. E.; Louie, S. G. *Phys. Rev. Lett.* **2010**, *105*, 266806.
- (22) Pesin, D.; MacDonald, A. H. *Nat. Mater.* **2012**, *11*, 409–416.
- (23) Brune, C.; Roth, A.; Buhmann, H.; Hankiewicz, E. M.; Molenkamp, L. W.; Maciejko, J.; Qi, X.-L.; Zhang, S.-C. *Nat. Phys.* **2012**, *8*, 485–490.
- (24) Modak, S.; Sengupta, K.; Sen, D. *Phys. Rev. B* **2012**, *86*, 205114.
- (25) Aseev, P. P.; Artemenko, S. N. *JETP Lett.* **2013**, *98*, 285–288.
- (26) Li, H.; Zhang, H. B.; Shao, J. M.; Zhang, Y. Y.; Yao, D. X.; Yang, G. W. *Appl. Phys. Lett.* **2012**, *101*, 243102.
- (27) McIver, J. W.; Hsieh, D.; Steinberg, H.; Jarillo-Herrero, P.; Gedik, N. *Nat. Nanotechnol.* **2012**, *7*, 96–100.
- (28) Jozwiak, C.; Park, C.-H.; Gottlieb, K.; Hwang, C.; Lee, D.-H.; Louie, S. G.; Denlinger, J. D.; Rotundu, C. R.; Birgeneau, R. J.; Hussain, Z.; Lanzara, A. *Nat. Phys.* **2013**, *9*, 293–298.
- (29) Park, C.-H.; Louie, S. G. *Phys. Rev. Lett.* **2012**, *109*, 097601.
- (30) Li, C. H.; van't Erve, O. M. J.; Robinson, J. T.; Liu, Y.; Li, L.; Jonker, B. T. *Nat. Nanotechnol.* **2014**, *9*, 218–224.
- (31) Hong, S.; Diep, V.; Datta, S.; Chen, Y. P. *Phys. Rev. B* **2012**, *86*, 085131.
- (32) He, L.; Kou, X.; Wang, K. L. *Phys. Status Solidi RRL* **2013**, *7*, 50–63.
- (33) King, P. D. C.; Hatch, R. C.; Bianchi, M.; Ovsyannikov, R.; Lupulescu, C.; Landolt, G.; Slomski, B.; Dil, J. H.; Guan, D.; Mi, J. L.; Rienks, E. D. L.; Fink, J.; Lindblad, A.; Svensson, S.; Bao, S.; Balakrishnan, G.; Iversen, B. B.; Osterwalder, J.; Eberhardt, W.; Baumberger, F.; Hofmann, P. *Phys. Rev. Lett.* **2011**, *107*, 096802.
- (34) Fert, A.; Jaffrès, H. *Phys. Rev. B* **2001**, *64*, 184420.
- (35) Yu, X.; He, L.; Lang, M.; Jiang, W.; Xiu, F.; Liao, Z.; Wang, Y.; Kou, X.; Zhang, P.; Tang, J.; Huang, G.; Zou, J.; Wang, K. L. *Nanotechnology* **2013**, *24*, 015705.
- (36) Zhang, Y.; He, K.; Chang, C.-Z.; Song, C.-L.; Wang, L.-L.; Chen, X.; Jia, J.-F.; Fang, Z.; Dai, X.; Shan, W.-Y.; Shen, S.-Q.; Niu, Q.; Qi, X.-L.; Zhang, S.-C.; Ma, X.-C.; Xue, Q.-K. *Nat. Phys.* **2010**, *6*, 584–588.
- (37) Lang, M.; He, L.; Xiu, F.; Yu, X.; Tang, J.; Wang, Y.; Kou, X.; Jiang, W.; Fedorov, A. V.; Wang, K. L. *ACS Nano* **2011**, *6*, 295–302.
- (38) Kong, D.; Cha, J. J.; Lai, K.; Peng, H.; Analytis, J. G.; Meister, S.; Chen, Y.; Zhang, H.-J.; Fisher, I. R.; Shen, Z.-X.; Cui, Y. *ACS Nano* **2011**, *5*, 4698–4703.
- (39) Tombros, N.; Jozsa, C.; Popinciuc, M.; Jonkman, H. T.; van Wees, B. J. *Nature* **2007**, *448*, 571–574.
- (40) Valenzuela, S. O.; Tinkham, M. *Nature* **2006**, *442*, 176–179.
- (41) Jönsson-Åkerman, B. J.; Escudero, R.; Leighton, C.; Kim, S.; Schuller, I. K.; Rabson, D. A. *Appl. Phys. Lett.* **2000**, *77*, 1870–1872.
- (42) Jedema, F. J.; Heersche, H. B.; Filip, A. T.; Baselmans, J. J. A.; van Wees, B. J. *Nature* **2002**, *416*, 713–716.
- (43) Odom, B.; Hanneke, D.; D'Urso, B.; Gabrielse, G. *Phys. Rev. Lett.* **2006**, *97*, 030801.
- (44) Tang, J.; Wang, C.-Y.; Chang, L.-T.; Fan, Y.; Nie, T.; Chan, M.; Jiang, W.; Chen, Y.-T.; Yang, H.-J.; Tuan, H.-Y.; Chen, L.-J.; Wang, K. L. *Nano Lett.* **2013**, *13*, 4036–4043.
- (45) Nagaosa, N.; Sinova, J.; Onoda, S.; MacDonald, A. H.; Ong, N. P. *Rev. Mod. Phys.* **2010**, *82*, 1539–1592.
- (46) Gould, C.; Rüster, C.; Jungwirth, T.; Girgis, E.; Schott, G. M.; Giraud, R.; Brunner, K.; Schmidt, G.; Molenkamp, L. W. *Phys. Rev. Lett.* **2004**, *93*, 117203.
- (47) Analytis, J. G.; McDonald, R. D.; Riggs, S. C.; Chu, J.-H.; Boebinger, G. S.; Fisher, I. R. *Nat. Phys.* **2010**, *6*, 960–964.
- (48) He, L.; Xiu, F.; Yu, X.; Teague, M.; Jiang, W.; Fan, Y.; Kou, X.; Lang, M.; Wang, Y.; Huang, G.; Yeh, N.-C.; Wang, K. L. *Nano Lett.* **2012**, *12*, 1486–1490.
- (49) Hikami, S.; Larkin, A. I.; Nagaoka, Y. *Prog. Theor. Phys.* **1980**, *63*, 707–710.
- (50) Bao, L.; He, L.; Meyer, N.; Kou, X.; Zhang, P.; Chen, Z.-g.; Fedorov, A. V.; Zou, J.; Riedemann, T. M.; Lograsso, T. A.; Wang, K. L.; Tuttle, G.; Xiu, F. *Sci. Rep.* **2012**, *2*, 726.
- (51) Lou, X.; Adelman, C.; Crooker, S. A.; Garlid, E. S.; Zhang, J.; Reddy, K. S. M.; Flexner, S. D.; Palmstrom, C. J.; Crowell, P. A. *Nat. Phys.* **2007**, *3*, 197–202.
- (52) Castro Neto, A. H.; Guinea, F.; Peres, N. M. R.; Novoselov, K. S.; Geim, A. K. *Rev. Mod. Phys.* **2009**, *81*, 109–162.
- (53) Tsymbal, E. Y.; Mryasov, O. N.; LeClair, P. R. *J. Phys.: Condens. Matter* **2003**, *15*, R109–R142.
- (54) Dash, S. P.; Sharma, S.; Le Breton, J. C.; Peiro, J.; Jaffrès, H.; George, J. M.; Lemaître, A.; Jansen, R. *Phys. Rev. B* **2011**, *84*, 054410.